



Inspection of nuclear assets with limited access using Feature Guided Waves

Euan A. Foster^{a,*}, Robert Bernard^b, Gary Bolton^c, Joseph C. Jackson-Camargo^a, Anthony Gachagan^a, Ehsan Mohseni^a, Charles N. MacLeod^a

^a University of Strathclyde, 16 Richmond St, Glasgow, G1 1XQ, UK

^b Sellafield Ltd, Sellafield, Cumbria, CA20 1PG, UK

^c National Nuclear Laboratory (NNL) Ltd, Havelock Rd, Workington, CA14 3YQ, UK

ARTICLE INFO

Keywords:

Guided ultrasonic waves
Feature guided waves
Nuclear inspection
Weld inspection

ABSTRACT

Resistance Seam Welding (RSW) is frequently used in many industries where low-cost mass manufacturing of gas/fluid-tight seals are required. One particular use case is in the fabrication of canisters to store nuclear material. Given the expected long lifetime and high replacement cost associated with nuclear infrastructure, it is common for an increase in the design life to be sought during operation. This leads to a need to integrate Non-Destructive Testing (NDT) techniques in a complex environment which frequently has accessibility issues. For the inspection of RSW nuclear canisters, one promising solution is to use Feature Guided Waves (FGWs) to rapidly screen the whole circumferential RSW joint from only partial circumferential access to ensure safe storage and targeted repackaging. FGWs can travel long distances while locally confining their energy to a topological feature such as a weld or stiffener. This paper explores such use of FGWs through both theoretical and practical experimental methods. To understand which FGW modes exist in the RSW joint, the Semi-Analytical Finite Element (SAFE) method was used, revealing four suitable wave modes. An anti-symmetric flexural RSW guided mode was down-selected due to its ease of excitation, intense energy concentration around the RSW, low dispersion and attenuation. Three-dimensional Finite Element (FE) simulations were conducted to explore the sensitivity of the flexural FGW to transverse cracks of differing dimensions. Experimental results on simplified and realistic geometries to transverse crack defects of ≥ 1 mm deep show the efficacy of using this method to efficiently screen nuclear canister RSW joints for such defects in-situ.

1. Introduction

“Welding” as a term can be defined as the process by which two or more pieces of metal are united under the influence of heat to form a homogeneous junction. This definition encases all welding processes and does not define any method to achieve such a structure [1].

Fusion welding is one ubiquitous process, which uses heat and no application of force to liquefy and unite the two workpieces as solidification occurs. In contrast, resistance welding is defined as the union of two workpieces under high pressure where the junction is formed when in a plastic state. It is important to note that no liquefaction occurs in resistance welding.

In resistance welding, the workpieces are clamped together between two electrodes and electricity is pulsed between them. The application of pressure and heat via current allows for a small volume of material to

coalesce together and form what is known as a weld nugget. Resistance welding can be further divided into two main subsets – spot and seam welding. In resistance spot welding, the electrodes are stationary and only form a singular nugget of merged material between the two workpieces over a localised region. By comparison, resistance seam welding utilises cylindrical electrodes which rotate and feed the two workpieces through them as current is pulsed, creating a welded seam of overlapping nuggets over a large area.

Typical resistance seam welding flaws occur in the fusion and/or the heat-affected zone and can occur at manufacture or while in service [2, 3]. Oversized/undersized nuggets [4], voids/porosity [5], expulsion [6], and transverse cracking [7] are the most widely reported defects and are graphically illustrated in Fig. 1. This study is primarily concerned with the detection of transverse cracks as they are the most detrimental to the overall structure.

* Corresponding author.

E-mail address: e.foster@strath.ac.uk (E.A. Foster).

It is common to use Resistance Seam Welds (RSWs) to establish a gas-tight or fluid-tight joint in sheet metal fabrications. Examples include fuel tanks in motor vehicles, tin cans, and steel drums. Steel drums with RSWs sealing the cylindrical body to the lid have been utilised to store nuclear material in the UK for several decades. Fig. 2 illustrates the RSW process, the resulting undulating RSW structure and a photograph as well as a CAD schematic of the cylindrical RSW used on canisters to store nuclear material.

It can be seen from Fig. 2 (d) that the nuclear canister RSW is offset from the top of the canister body and can be thought of as a cylindrical lap joint. As the aforementioned fusion and heat-affected zones are at the unification between the canister body and lid, these zones become structurally critical in the resulting component. Being able to inspect these structurally important areas for defects after manufacture and while in service is of high priority for safety-conscious industries such as the nuclear industry [8].

Traditionally, the inspection of nuclear canisters and their welds has been highly challenging, time-consuming, and expensive. This inspection challenge is complicated further when the asset lifetime exceeds the original design intent, and when storage facilities obstruct access to the canister itself. This problem is one that is currently being faced in the UK, where government policy has shifted from favouring reprocessing to long term storage of nuclear assets [9]. Additionally, the storage facilities are often designed with long-term storage and inspection not in mind. Thus, gaining access to the assets whilst in storage is challenging. An example storage facility is depicted in Fig. 3, where access to the canisters is given through access ports on one side of the storage structure. Partial circumferential access to the canister welds is provided through one of two channels. Therefore, a bespoke Non-Destructive Testing (NDT) technique focusing on the RSW that screens the whole circumferential weld for defects from only partial circumferential access would be beneficial to ensure continued safe storage.

Ultrasonic guided wave testing has long been an attractive method for rapidly screening components inaccessible to the user from a single remote transducer position [10]. However, in recent years, a feature trapping effect that confines the ultrasonic guided wave propagation

within a particular topological feature in a component has been discovered [11] and exploited extensively [12–20]. Due to the change in geometry around a structural feature, it has been shown that local Feature Guided Waves (FGWs) exist in complex structures such as fusion welds [12–15], bends [16–18], seal fins [19] and stiffeners [20]. This phenomenon can be explained due to the change in geometry of the local feature, creating guided wave modes that possess similar mode shapes but different phase velocities to that of the adjacent structure, due to the total internal reflection of the wave as it propagates along the feature [21]. Therefore, FGWs are a highly attractive NDT modality that offers rapid long-range screening of obscured features and is well suited to the inspection of RSWs located on nuclear canisters whilst in storage.

Different mode shape categories of FGWs have been exploited in literature for differing non-destructive testing scenarios. Fan & Lowe [12] initially discovered four fundamental mode shape categories (flexural, torsional, longitudinal, & shear horizontal) for a fusion weld. It has since been shown that the shear horizontal feature guided mode, with its lower levels of attenuation and dispersion, offers much promise for the screening of fusion welds [14]. This has been confirmed and expanded on by Yu et al. [15] in which a novel signal processing technique was utilised to significantly increase the reflection of high order weld guided shear horizontal FGWs from axial and transverse cracks of 20% wall thickness. Stemming from this success, other publications have also made use of shear horizontal FGWs. Shear horizontal FGWs have been shown to effectively screen transverse and axial defects in rolled flat plate structures [17], as well as disbonds in an adhesive layer between composites and stiffeners [20].

More recently, other mode shape categories have been exploited. Corcoran et al. [19] demonstrated that flexural antisymmetric FGWs could be used to detect 0.75 mm EDM notched defects in seal fins. Manogharan et al. [18] showed that longitudinal FGWs can be used to screen curved composite stringer joints. While Ramdhas et al. [16] have shown that antisymmetric FGWs can be used to also screen for defects on rolled flat plate structures. It can be summarised that the ideal mode shape of FGW used for a particular application will have high energy concentration in the feature under inspection accompanied by low levels

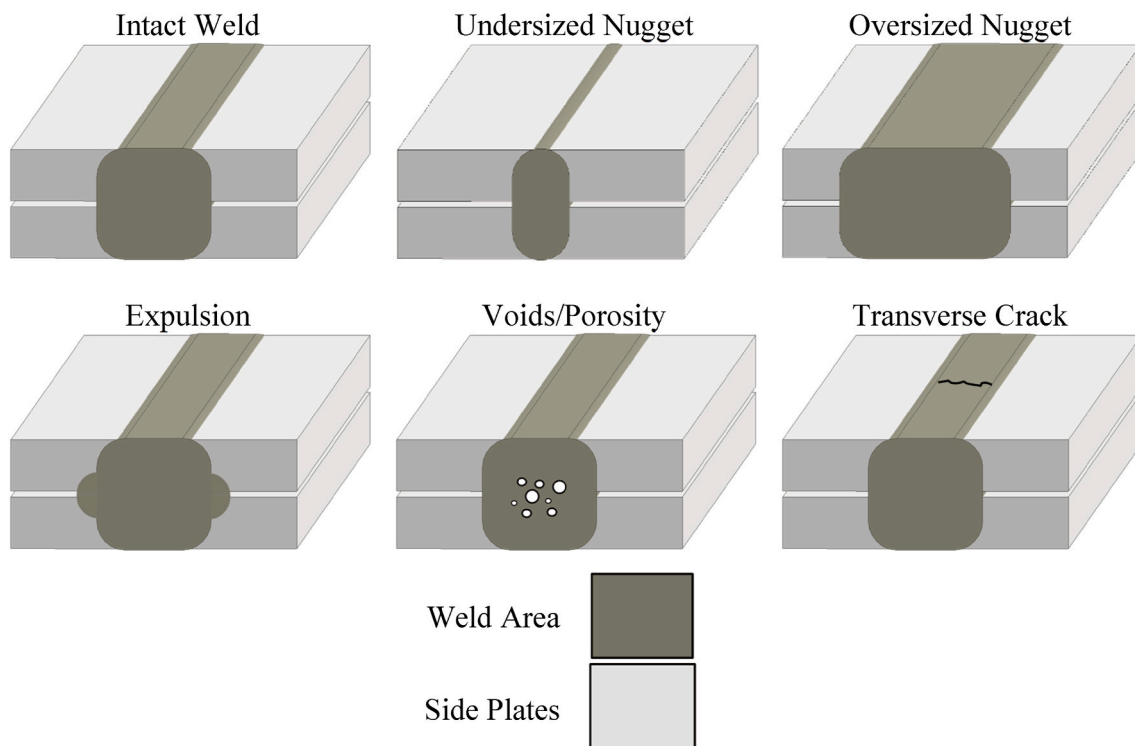


Fig. 1. Illustrations of most common RSW defects in a cross-section view.

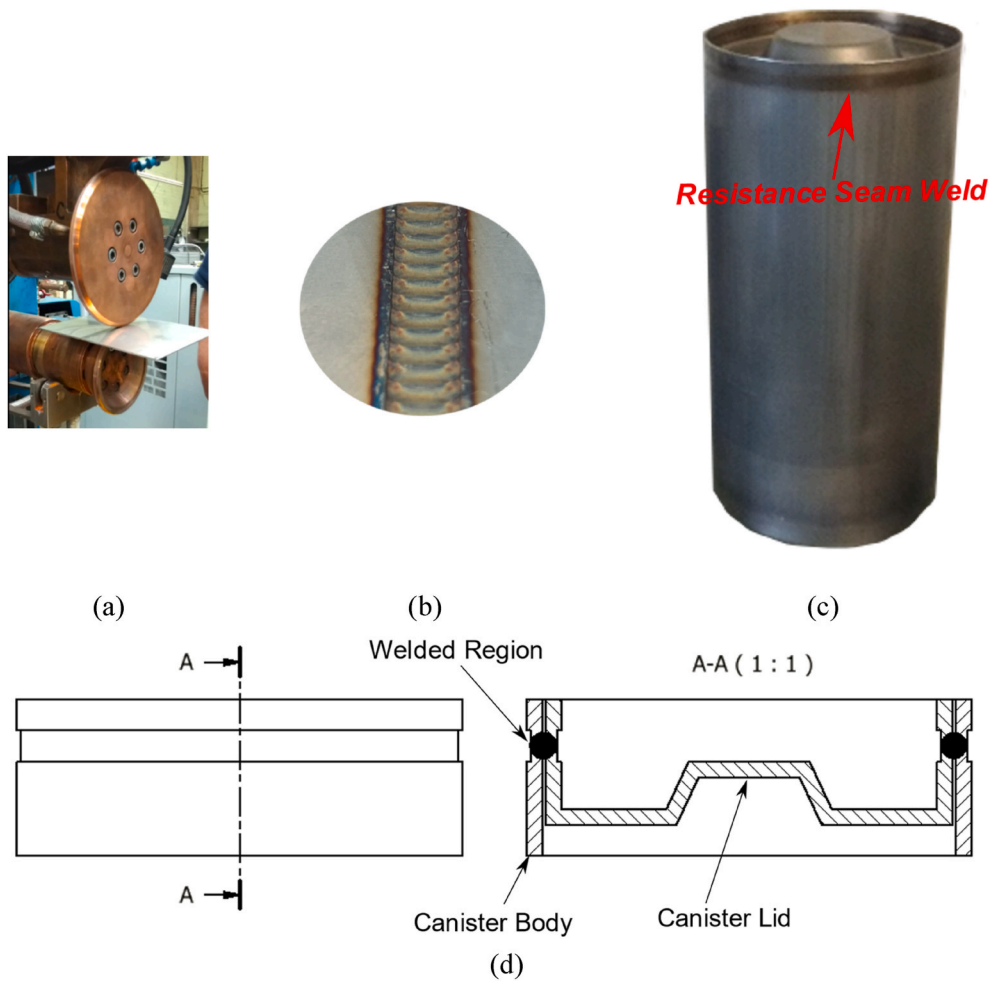


Fig. 2. Resistance seam welds (a) Welding process, (b) Close-up of weld structure, (c) Welded cylindrical RSW canister, (d) CAD schematic and cross-sectional view of RSW canister.

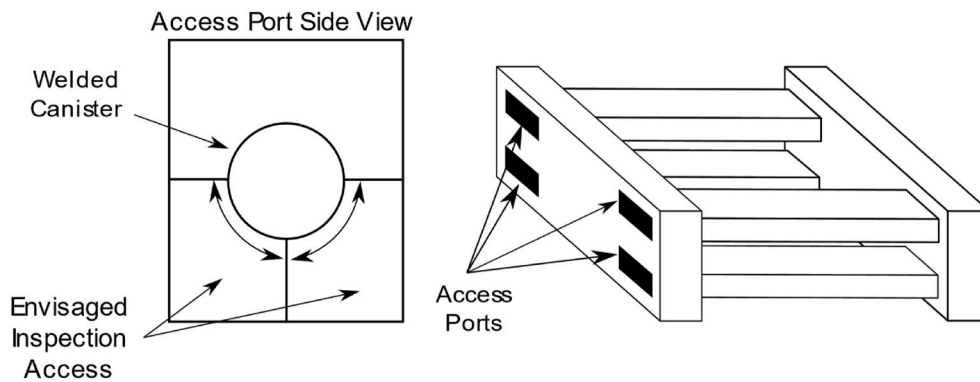


Fig. 3. Schematic of cannister storage facility.

of attenuation, and will vary as a function of the material and the geometry of the component.

This paper presents the simulation and experimental verification activities focussed on the concept and deployment of a FGW within a nuclear canister RSW. Firstly, to determine suitable FGW modes, a modal study of the RSW geometry using the Semi-Analytical Finite Element (SAFE) method [22], which accurately predicts the existence of guided waves within arbitrary cross-sections, was performed. From the SAFE model, multiple FGW modes were predicted to exist in these RSWs, along with their associated dispersive properties. Down selection of the

identified modes was undertaken, where low attenuation and high energy concentration were the key requirements, resulting in one mode being selected for further study. The interaction of the selected mode with defects was then studied via Finite Element (FE) simulations and validated by experimental measurements on both simplified and real-world RSWs. It was shown that analytical solvers could be used to predict the existence of FGWs for simplified geometries accurately. For real-world RSWs, it was also shown that the SAFE method could be used to accurately predict the existence of FGWs. Moreover, the practical deployment of FGWs through the development of a prototype system

that could effectively screen for defects on both flat and cylindrical RSWs is demonstrated for the first time. Lastly, the paper concludes with the aims for the future development of this work.

2. Modal analysis of the RSW joint using SAFE approaches

2.1. SAFE modelling

The well-established SAFE method was employed to identify and understand the dispersive properties of the guided wave modes that

exist in a resistance seam welded canister. The SAFE method solves the quadratic eigenvalue problem of a solid with a constant arbitrary cross-section and assumes a harmonic oscillation along the direction of propagation. As a result, the SAFE method only requires the discretisation of the 2D cross-section. Castaings and Lowe [23] developed the SAFE method to incorporate leaky guided waves along an elastic waveguide with an arbitrary cross-section radiating into a solid of infinite extent. Therefore, the wave number returned for a given frequency is complex, where the real component corresponds to the angular wavenumber of a propagating wave, and the imaginary

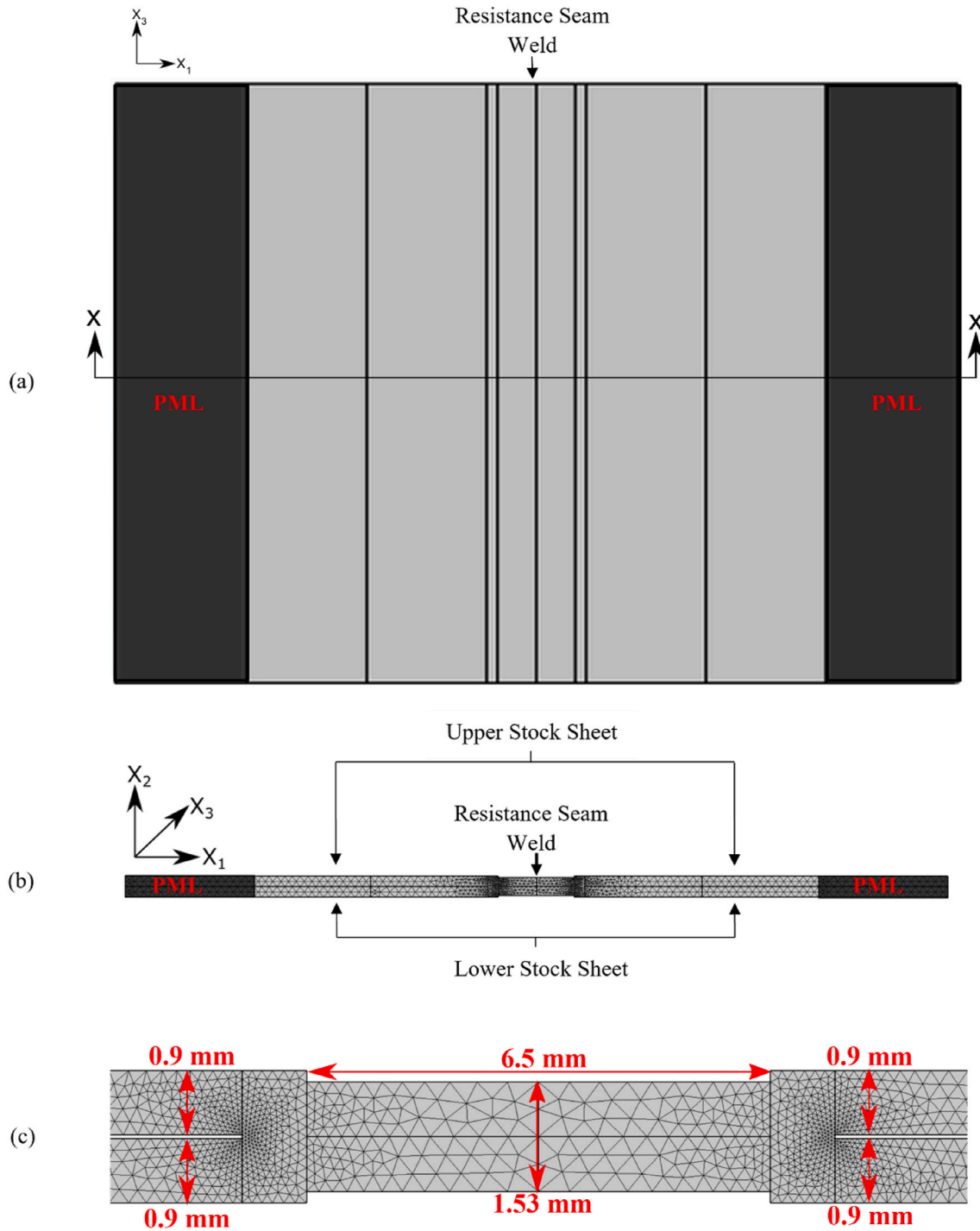


Fig. 4. Schematic of SAFE model geometry (a) Plan view of RSW component with cross-sectional arrows. (b) 2-Dimensional cross-sectional view of the discretised SAFE model geometry detailing the RSW and stock sheets. Stock sheets either side of the weld are separated by a 0.05 mm air gap. (c) Detailed view of the 2-Dimensional cross-sectional discretised SAFE model geometry detailing relevant dimensions taken from the CT scan.

component corresponds to the attenuation characteristics of any leakage present in the feature guided waves predicted in nepers per meter.

In this paper, the SAFE method was implemented on the commercial FE package, COMSOL [24]. The eigenvalue search was performed with a centre root search around $k = \frac{2\pi f}{c_T}$, and the number of roots was gradually increased to 700 until no additional modes of interest were returned, thus indicating convergence had been met. The SAFE method applied to a flat plate was used for this cylindrical structure. It has been shown within literature [25–27] that the dispersion relationships for flat plates match those of circumferential propagation under certain geometric conditions. These conditions include the inner to outer radius ratio being approximately equal to one and the thickness to radius ratio being less than 10%. The proposed canister structure fits well within these criteria; therefore, the solutions produced by this flat plate analysis were applied to the curved canister structure.

A schematic of the simplified RSW cross section used in the SAFE model is shown in Fig. 4 where the weld's length is extended along the x_3 direction which is perpendicular to the 2-dimensional domain of the problem. The model contains three distinct regions. The central region is the RSW, which has a thickness and width of 1.53 mm and 6.5 mm, respectively. Either side of the RSW are the unwelded stock sheets which are 0.9 mm thick, separated by a very small (0.05 mm) air gap. This simplified geometry was extracted from an X-ray CT scan of a RSW sample where undulations in the weld were noted to occur ~6 mm in the axial direction. Finally, at the perimeter of the model, there is an 11 mm wide Perfectly Matched Layer (PML). This is in line with the guidance given by Zuo et al. [28], where the minimum angular wavenumber in the frequency range of interest is the dominant factor in determining the PML length. By introducing the PMLs, the real coordinates of the physical equations are extended into the complex domain allowing standing waves to be absorbed. Therefore, standing non-propagating waves are not present in the solutions generated by the SAFE model. Nyugen et al. provide further information on how PMLs are practically implemented within SAFE modelling [29].

The entire geometry was assigned the elastic moduli associated with 316 stainless steel [30] ($\rho = 7958 \frac{\text{kg}}{\text{m}^3}$, $E = 194.62 \text{ GPa}$, $G = 75.2 \text{ GPa}$). The mesh was composed of 1710 quadratic triangular Lagrangian elements, and the model was solved from a minimum frequency of 50 kHz to a maximum frequency of 1 MHz in steps of 10 kHz to ensure resolution and accuracy over a suitable frequency window.

2.2. FGW mode selection

To select a suitable FGW mode and operational frequency for inspection, the modal solutions generated by the SAFE method were investigated. The axial component of the time averaged power flow in the x_3 direction can be calculated at the nodal points of the mesh for all modes identified using the following formula [21]:

$$P_{x_3} = -\text{Re} \left[\left(\frac{I\omega}{2} \right) (U_1^* \sigma_{31} + U_2^* \sigma_{32} + U_3^* \sigma_{33}) \right], I = \sqrt{-1} \quad \text{Eq. 1}$$

where σ_{31} , σ_{32} and σ_{33} are the components of axial stress; U_1^* , U_2^* and U_3^* are the complex conjugates of displacement. To obtain the averaged domain axial power flow, it is necessary to integrate over the domain of interest according to the following, where S denotes the cross-sectional area.

$$\bar{P}_{x_3} = \frac{\int_S |P_{x_3}| ds}{\int_S ds} \quad \text{Eq. 2}$$

Suitable FGW modes are identified where the average power flow is

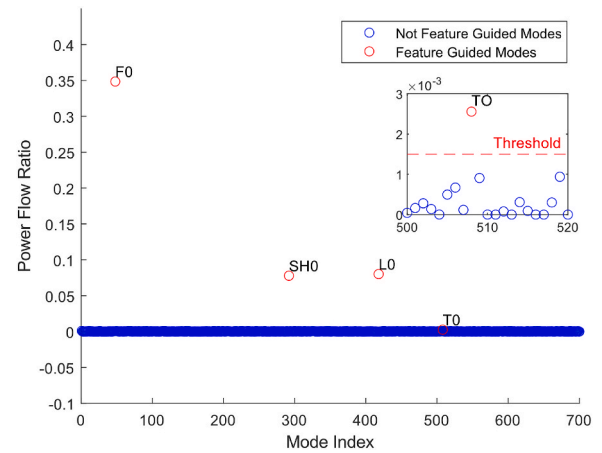


Fig. 5. Power flow ratio at 100 kHz with 700 Eigenvalues.

higher in the feature of interest than that of the surrounding structure. The power flow ratio that describes this scenario can be calculated by the following formula:

$$\eta = \frac{\bar{P}_{x_3 \text{ guide}}}{\bar{P}_{x_3 \text{ total}}} \quad \text{Eq. 3}$$

Fig. 5 shows the power flow ratio for all eigenvalue solutions given from the SAFE model at 100 kHz. It can clearly be seen that when there is strong energy confinement in the RSW, the power flow ratio peaks and subsequently can be used to filter out solutions that are not weld guided as established by Zuo et al. [28]. By leveraging this property in combination with a proprietary algorithm, automatic detection of unique FGW modes and their corresponding dispersive properties was performed across the entire frequency spectrum of this problem.

Fig. 6 shows the axial power flow, normalised orthogonal displacements, and vibrational pattern (indicated by arrows) that contribute to the through thickness mode shapes of the four-wave modes identified from this analysis at various frequencies. These details allow the identified wave modes to be classified based on the dominant displacement of their mode shape and vibrational pattern. For instance, Fig. 6 (c) shows a mode shape dominated by the shear displacement component and was hence classified as the fundamental Shear Horizontal (SH_0) weld guided mode. Fig. 6 (i) shows a mode shape dominated by axial displacement component and was classified as the fundamental Longitudinal (L_0) weld guided mode. Fig. 6 (f) shows a mode shape dominated by the shear displacement component but has a rotational vibrational pattern and was denoted as the fundamental Torsional (T_0) weld guided mode as a result. As torsional wave modes predominantly exist only in pipes, this result is more characteristic of a pipe rather than that of a plate. Lastly, Fig. 6 (l) shows a mode shape dominated by the vertical displacement component and was termed the fundamental Flexural (F_0) weld guided mode.

Fig. 6 also shows how the attenuation of the identified wave modes is characterised by changes in the axial power flow over the frequency spectrum of this problem. Fig. 6 (a), (d), (g) & (j) show points of relatively high attenuation of the fundamental SH_0 , T_0 , L_0 , and F_0 weld guided modes, respectively. While Fig. 6 (b), (e), (g) & (k) show points of relatively low attenuation of the fundamental SH_0 , T_0 , L_0 , and F_0 weld guided modes respectively. It can be seen that as the attenuation decreases, a stronger energy trapping effect is observed on the aforementioned contour plots.

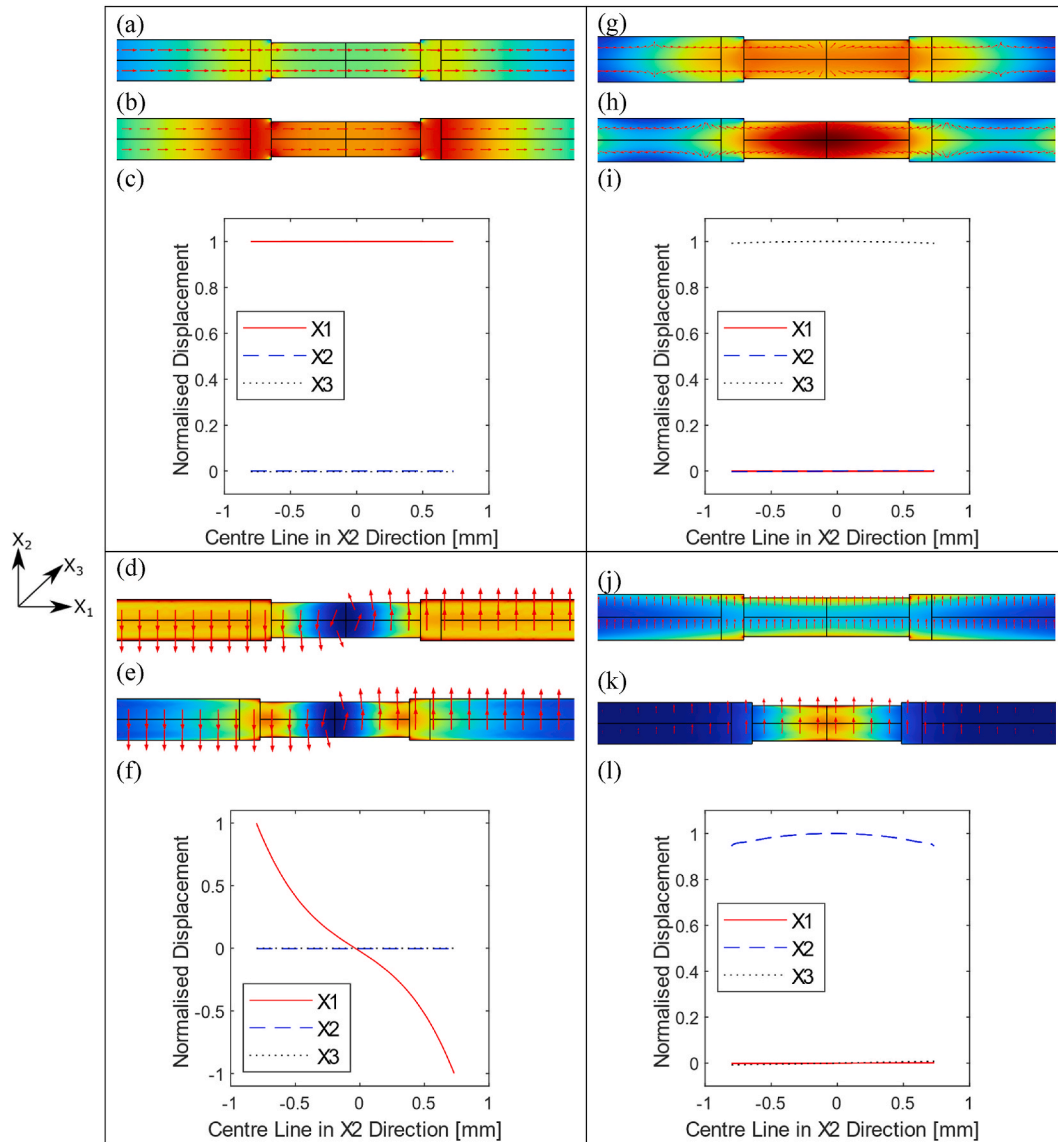


Fig. 6. Axial power flow contour plots, vibrational pattern (indicated by arrows) & mode shapes of weld guided wave modes predicted by the SAFE method (a) SH_0 like power flow at 400 kHz ($\alpha = 0.154$ Np/m), (b) SH_0 like mode power flow at 900 kHz ($\alpha = 0.0148$ Np/m), (c) SH_0 like mode shape at 400 kHz, (d) T_0 like mode power flow at 600 kHz ($\alpha = 0.265$ Np/m), (e) T_0 like mode power flow at 900 kHz ($\alpha = 1.888 \times 10^{-4}$ Np/m), (f) T_0 like mode shape at 600 kHz, (g) L_0 like mode power flow at 270 kHz ($\alpha = 0.539$ Np/m), (h) L_0 like mode power flow at 400 kHz ($\alpha = 0.468$ Np/m), (i) L_0 like mode shape at 270 kHz, (j) F_0 like power flow at 60 kHz ($\alpha = 0.0768$ Np/m), (k) F_0 like power flow at 900 kHz ($\alpha = 0$ Np/m), (l) F_0 like mode shape at 60 kHz. The colour coding represents the relative amplitude of the axial power flow of each guided mode at particular frequencies (blue: low to red: high). (For interpretation of the references to colour in this figure legend, the reader is referred to the Web version of this article.)

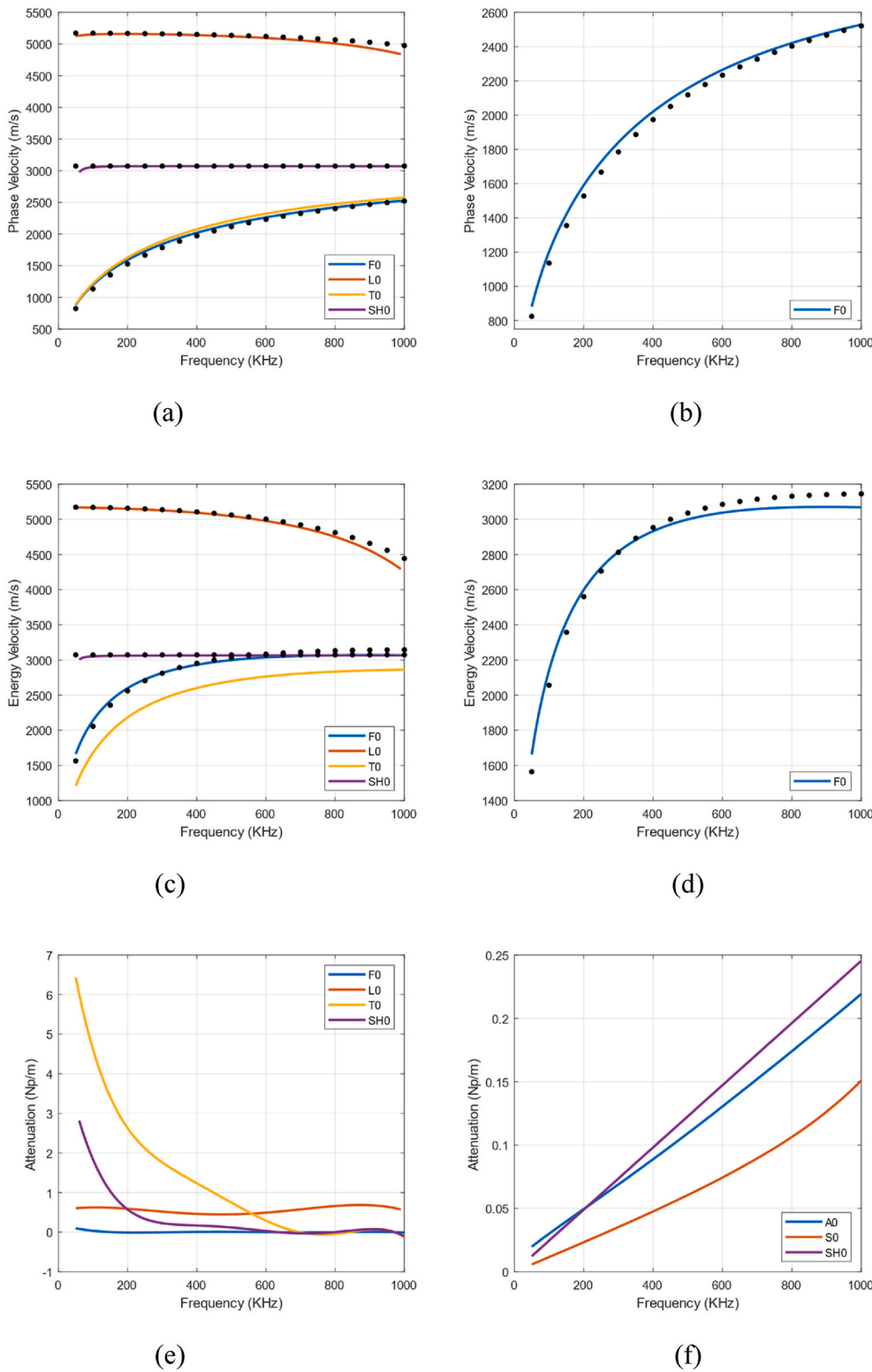


Fig. 7. Dispersion characteristics of identified weld guided modes and their analytical counterparts for a free plate of the same thickness as the weld (1.53 mm, $\rho = 7958 \text{ kg/m}^3$, $E = 194.62 \text{ GPa}$, $G = 75.2 \text{ GPa}$, $\alpha_L = 0.002 \text{ Np}/\lambda$, $\alpha_T = 0.004 \text{ Np}/\lambda$) (a) Phase velocity of all weld guided modes, (b) Phase velocity of F_0 weld guided mode (c) Energy velocity of all weld guided modes, (d) Energy Velocity of F_0 weld guided modes, (e) Attenuation of all weld guided modes automatically detected from the SAFE solutions, (f) Attenuation of conventional analytical solutions for a free plate of the same thickness as the weld. Where (...) represent conventional analytical solutions of the S_0 , SH_0 & A_0 modes propagating along a free plate of the same thickness as the weld.

Fig. 7 shows the variations in phase velocity, energy velocity, and attenuation of the wave modes identified with analytical solutions superimposed for a free plate of the same thickness as the weld. The F_0 , SH_0 , and L_0 weld guided modes are shown to be highly similar to that of the A_0 , SH_0 , and S_0 analytical free plate solutions for both phase and energy velocity. However, greater differences are observed in their energy velocity dispersion curves due to the presence of increased attenuation for the leaky weld guided modes compared to that of their

analytical counterparts. A trend also observed in the literature [12,23] and the work reported within this study is that any plate-like feature with a constant thickness different to that of the surrounding structure possesses similar FGWs to that of their analytical free plate counterparts. Therefore, it is expected that well documented traditional guided wave transduction techniques can also be utilised to successfully create the FGW of choice. Furthermore, it is hypothesised that this trend will hold for other components with similar plate-like features.

The attenuation dispersion curve shown in Fig. 7 (e) is quite different from what one may expect when considering the analytical equivalents shown in Fig. 7 (f). This result may appear counterintuitive initially, but several other FGW studies have reported similar attenuation characteristics. Manogharan et al. [17] reports a fundamental shear horizontal bend guided mode in which attenuation decreases as frequency increases - a trend that is also observed in this study. While Ramdhas et al. [16] report an antisymmetric bend mode that also exhibits low attenuation. Furthermore, Castaings and Lowe [23] report a highly unique attenuation dispersion curve for a weld guided S_0 mode that exhibits zero attenuation except from two distinct peaks. Their work demonstrates and explains that due to the Snell Descartes Law [21] the weld guided S_0 mode cannot radiate as either the SH_0 or A_0 mode of the adjacent plates at particular frequencies. This is due to the phase velocity of the SH_0 mode of the adjacent plates being larger than that of the S_0 weld guided mode, and the A_0 mode of the adjacent plates having a mode shape that is too dissimilar to that of the S_0 weld guided mode. By using the same logic and applying it to the work present within this study, it can be said that the F_0 weld guided mode, with its low phase velocity can only radiate as the A_0 mode of the adjacent plates. Moreover, the F_0 weld guided mode and A_0 mode of the adjacent plates possess highly similar mode shapes and therefore, the low attenuation characteristic of the F_0 weld guided mode in Fig. 7 (e) is expected and confirmed with variations in the axial power flow illustrations shown in Fig. 6.

As has been highlighted in the previous paragraphs, the F_0 weld guided wave mode possesses the highest axial power flow confined to the RSW region. On average, the power flow ratio of the F_0 weld guided mode is 5.25 times higher than the next highest wave mode identified. Due to the manufacturing process, this result was not unexpected as the geometry change is most significant in the weld's vertical axis, giving rise to a more substantial energy trapping effect. For experimental applications, a frequency of 1 MHz is recommended due to the abundance of commercially available transducers with this centre frequency and the lower dispersion characteristics observed at higher frequencies. In summary, the F_0 weld guided wave mode, with its high energy confinement in the RSW along with its low attenuation and low dispersion at higher frequencies, made it the most suitable candidate for screening of nuclear grade RSWs.

2.3. Evaluation of modal analysis via 3D FEA

Several three-dimensional explicit FE simulations were performed on the accelerated high-fidelity GPU-based FE package Pogo [31] to further verify the predictions from the SAFE method, investigate suitable transduction techniques, and gain insight into defect sensitivity. Pogo-Pro visualised the field outputs while MATLAB performed the analysis of the time and field histories.

Fig. 8 shows a schematic of the FE model domain and a snapshot of the displacement field magnitude, where a FGW confined to the RSW can be clearly seen. Fig. 8 also depicts energy radiating from the FGW on the RSW and a faster plate-guided wave in the unwelded side sheets. Other similar publications have noted similar results [14] and also note that low attenuation of a FGW is accompanied by an angle of radiation of $\sim 90^\circ$ [23].

The FE model used the same geometry described in Section 2.1, and the overall domain was 128.30 x 1.85 x 550.00 mm. The internal utility, pogoMesh, discretised the domain and the resulting mesh comprised of 43,747,000 C3D6R 6 node triangular prism elements with an average size of 0.2 mm. The C3D6R element was chosen due to its ability to mesh complex structures and due to the fact that it has been extensively used within literature to effectively simulate such problems [32–34]. The mesh size of 0.2 mm was chosen as it was smaller than 1/20th of the shortest wavelength in the medium [35]. In addition, a 50 mm Absorbing Region with Increasing Dampening (ALID) [17,18] was applied at the boundaries of the plate to limit the extent of the domain and effectively apply an unbounded boundary condition. A high-performance computer that contains two Nvidia GeForce RTX 3090 graphics cards solved each model in approximately 10 mins.

The initial models were excited at a broad range of frequencies utilising a sinc function with a cut-off frequency of 1.3 MHz. The properties of the sinc function are shown in Fig. 9. This function was applied on a singular node in the x_2 direction on the upper surface of the welded pocket to successfully launch the F_0 weld guided mode. Several displacement monitors logged the displacement on the central position on the upper surface of the weld in the x_2 direction from $x_3 = 100$ mm to $x_3 = 500$ mm in steps of 1 mm. The resulting array of displacements was analysed using a two-dimensional Fast Fourier Transform (2D-FFT) [25, 36]. It should be noted that the data was Hann windowed in both the

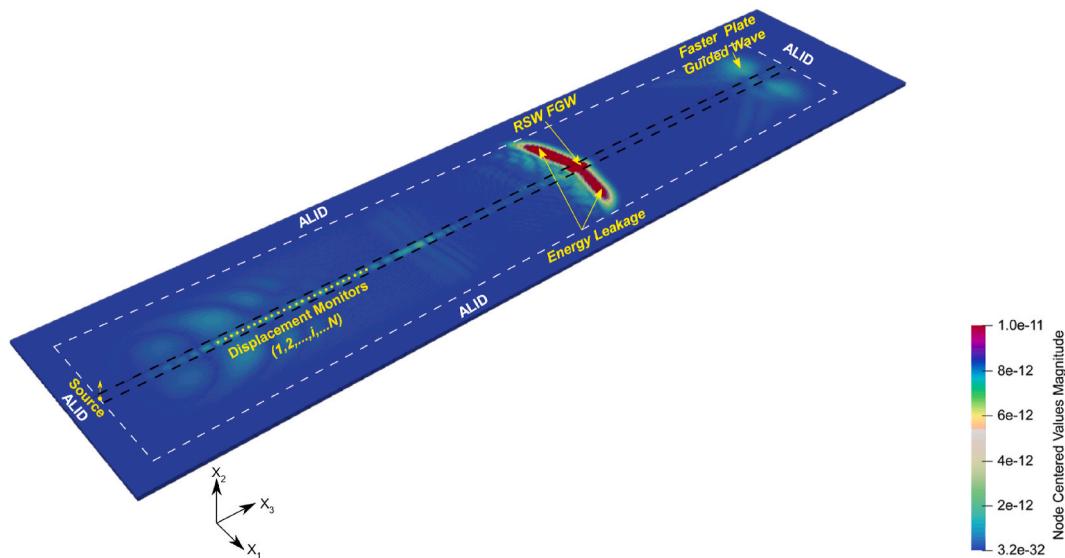


Fig. 8. 3D FE model schematic from a 5-cycle Hann windowed 1 MHz excitation signal showing the displacement field magnitude of the FGW travelling up the RSW surrounded by absorbing layers with increasing dampening (ALID).

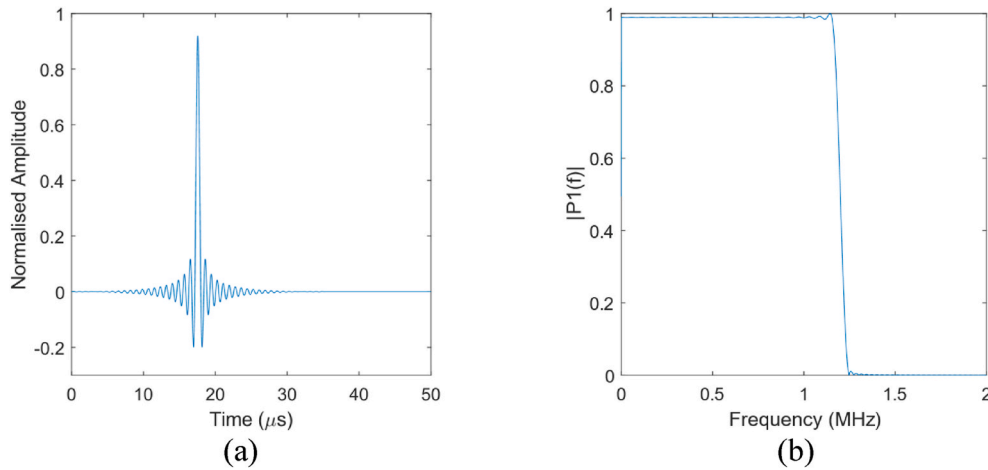


Fig. 9. Wideband sinc excitation function. (a) Time domain sinc function (b) Single-sided amplitude spectrum of (a).

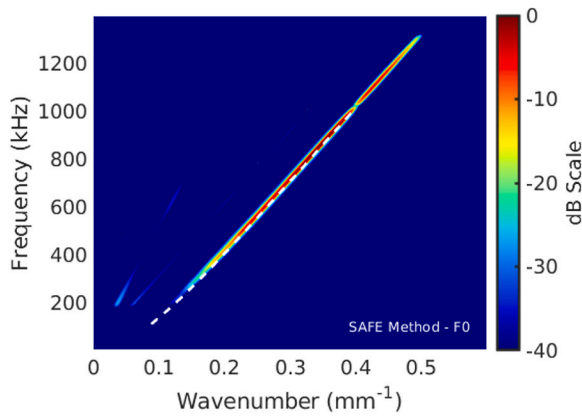


Fig. 10. Normalised wavenumber-frequency spectra.

space and time dimensions prior to performing the 2D-FFT to suppress discontinuities caused by the signal not being an integer number of periods for all wavenumbers present. The resulting spectra comprised of wavenumber-frequency data and is shown in Fig. 10 normalised by the maximum modulus on a dB scale.

The wideband excitation of the sinc function is clearly shown, and good alignment with the predictions from the SAFE model is observed. Additionally, other studies have shown that the excitation technique utilised in this model to generate such anti-symmetric flexural Lamb-like wave modes is well suited to experiments that employ the angle-incidence method as their transduction technique [37,38].

To further confirm the energy concentration effect, the same model was run with a 5-cycle 1 MHz Hann windowed excitation signal and studied in depth. The entire displacement field history at each nodal point was logged as well as the displacement time histories at the monitor points from $x_3 = 100$ mm to $x_3 = 500$ mm in steps of 1 mm. Fig. 11 shows an A-scan taken in the centre of the simulated plate at $x_3 = 225$ mm and clearly indicates the flexural weld guided mode as the dominant mode excited. The propagation time of $\sim 68 \mu\text{s}$ agrees with the SAFE energy velocity of 3068.4 m/s to cover a 225 mm transit.

Fig. 12 (a) shows the displacement field of a $x_{1,2}$ cross-sectional plane at a position of $x_3 = 225$ mm at $68 \mu\text{s}$ in time. The strong energy concentration effect can be observed along with the radiated A_0 wave in the stock side sheets. Moreover, Fig. 12 (b) plots the variation in the displacement field at the centre of the upper stock sheet. It can be seen that the displacement field exhibits a periodicity out with the central

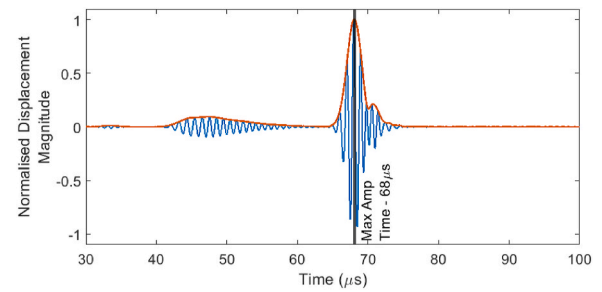


Fig. 11. A-scan of the displacement field at $x_3 = 200$ mm

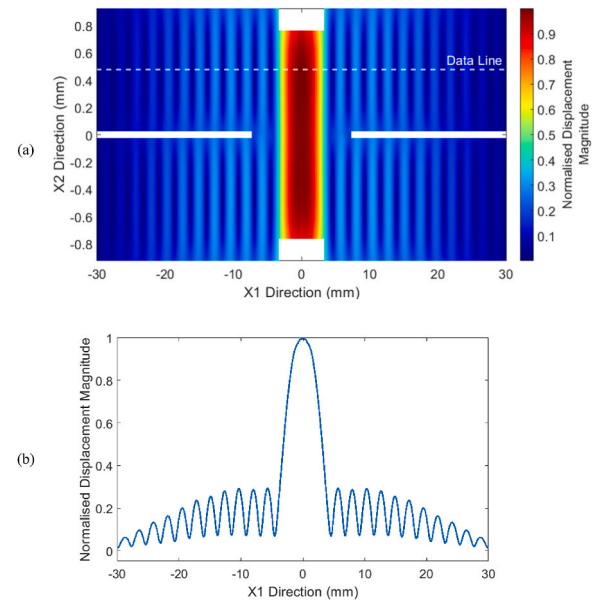


Fig. 12. Displacement field at $x_3 = 200$ mm at $68 \mu\text{s}$ from $-30 \leq x_1 \leq 30$ mm (a) Contour plot of the entire $x_{1,2}$ plane displacement field from $-30 \leq x_1 \leq 30$ mm (b) Normalised displacement field across the centre of the upper stock sheet from $-30 \leq x_1 \leq 30$ mm indicated by the dashed white line in Fig. 12(a).

welded region of 2.309 mm. As shown by Castaings and Lowe [23], this periodicity is indicative of the wavelength of the acoustic field being radiated from the FGW as it propagates along the feature. For a

wavelength of 2.309 mm at 1 MHz this gives a speed of 2309.39 m/s which approximately matches the phase velocity for the A_0 mode for a 0.9 mm steel sheet at 2306.51 m/s. These results confirm that the high energy concentration and low attenuation properties of the flexural weld guided mode predicted from the SAFE modelling in Section 2.1 & 2.2 are indeed observed in these initial time step FEA models and are in line with previously published literature.

2.4. Defect reflectivity

With successful models predicting and showing the presence of the fundamental flexural weld guided mode within the RSW, it was necessary to evaluate its sensitivity to defects. Therefore, various transverse cracks were introduced into the model by disconnecting adjacent nodes perpendicular to the crack extent. This location corresponded to a half circumferential transit of ~225 mm and was viewed as the maximum distance a defect could be from the transducer.

The same central node on the upper surface of the welded pocket was excited with a 5-cycle Hann-windowed 1 MHz toneburst signal. Likewise, displacement monitors logged the displacement from 100 mm to 200 mm in steps of 1 mm. An expansion of the 2D-FFT method previously mentioned was employed to generate the images denoted in Fig. 13.

As can be seen, both positive and negative wavenumbers are present within the spectra representing transmitted and reflected waves, respectively. With transmitted and reflected wave modes separated, it is then possible to calculate the reflection coefficient according to Eq. (4).

$$R(f_0) = 10^{\frac{A_r - A_i}{20}} \tag{Eq. 4}$$

where A_r and A_i are the reflected and incident amplitudes in dB space for a positive and negative wavenumber of identical magnitude.

Table 1
Crack dimensions and their corresponding reflection coefficients.

Crack Dimensions	Reflection Coefficient
Full Width, Full Depth – 6.500 x 1.530 mm	19.11%
Full Width, Half Depth – 6.500 x 0.765 mm	11.45%
Half Width, Full Depth – 3.250 x 1.530 mm	16.33%
Half Width, Half Depth – 3.250 x 0.765 mm	7.82%

Table 1 summarises the reflection coefficients obtained from several FE models where the crack width and height were modified. It can be concluded that the crack depth is the dominant factor when determining the reflection coefficient. Deeper cracks consistently produced significantly higher reflections. This trend is illustrated visually between Fig. 13 (b) & (c) in the wavenumber-frequency spectra.

3. Experimental validation

Several experiments were undertaken to initially verify the successful generation of the predicted flexural FGW and subsequently evaluate the efficacy of using this FGW to screen for defects. A flow chart of the experiments conducted with the hypotheses they were testing and the findings they generated is illustrated in Fig. 14.

Firstly, a machined aluminium pseudo weld was manufactured and experimented on. This simplified geometry removed the possibility of any unforeseen interactions with the undulating nature of the RSW and the propagating wavefront (See Fig. 2 (b)), while also removing any challenges associated with wave propagation within the core material [39]. Then, with further confidence developed in the experimental approach, additional experiments of increasing complexity were

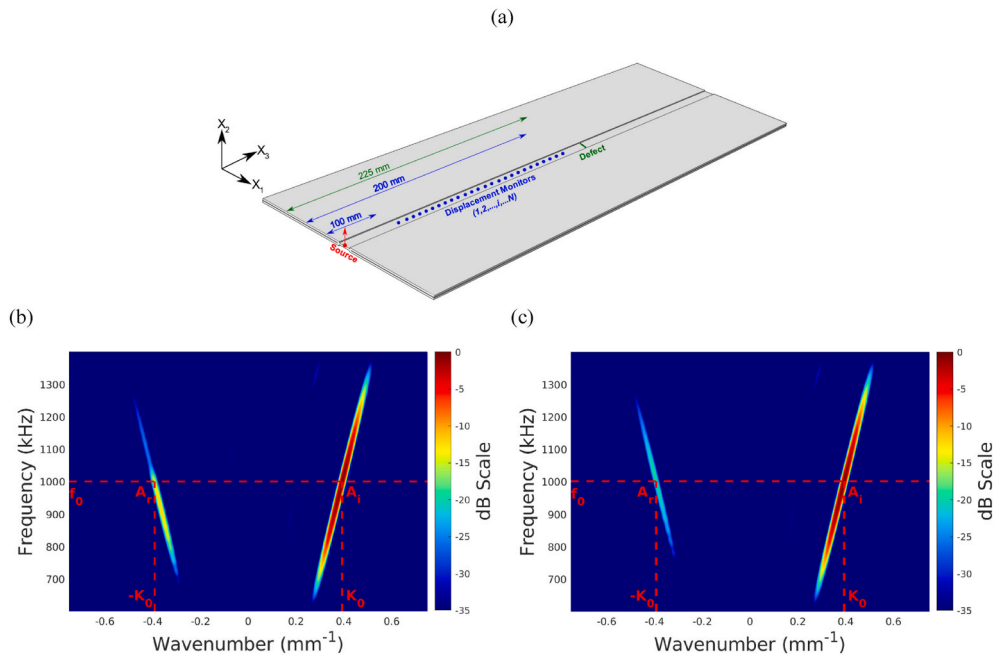


Fig. 13. (a) Schematic of FE model utilised to study the interaction of the F_0 RSW guided mode with defects, (b) Wavenumber-frequency spectra for a 5-cycle Hann-windowed 1 MHz excitation and 6.5x1.53 mm (full width full depth) crack at 225 mm (c) Wavenumber-frequency spectra for a 5-cycle Hann-windowed 1 MHz excitation and 6.5 × 0.765 mm (full width half depth) crack at 225 mm.

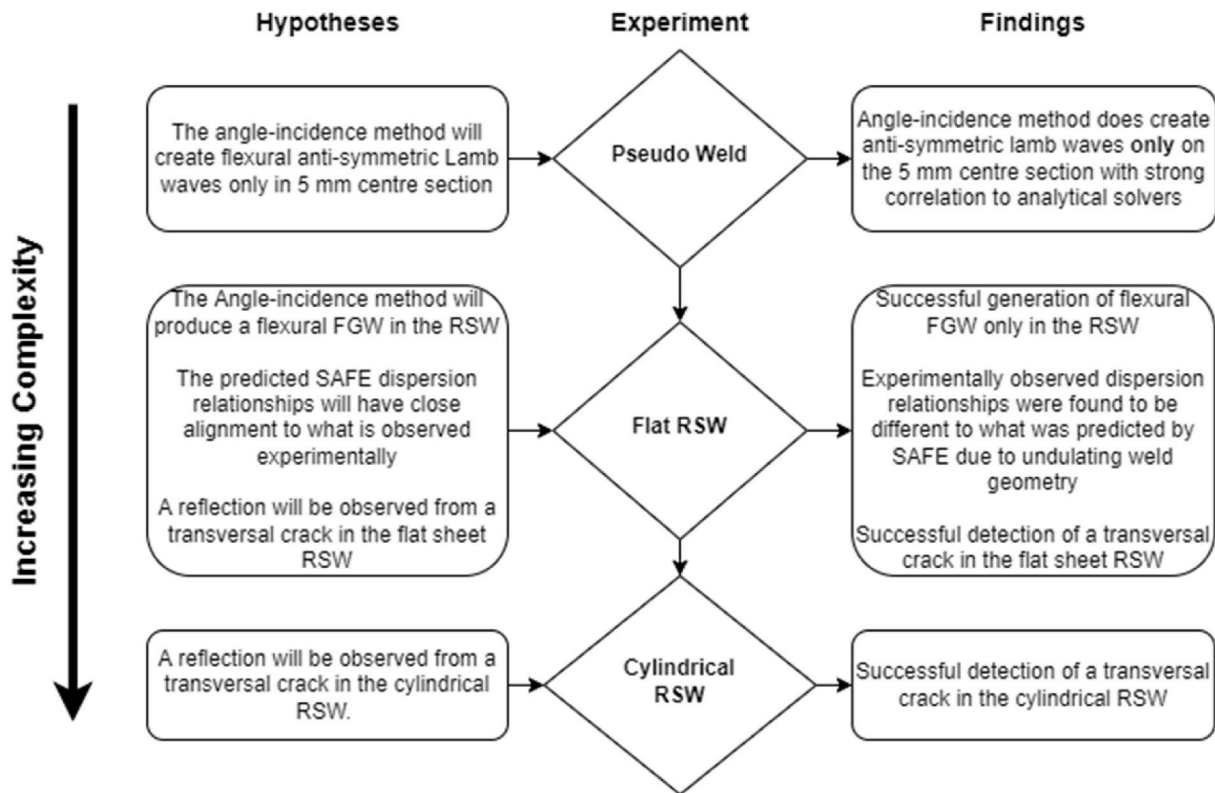


Fig. 14. Experimental flow chart showing the series of experiments undertaken.

conducted on flat and cylindrical stainless steel RSWs representative of the welds utilised on nuclear canisters.

3.1. Pseudo Weld

A simplified weld was machined from 6082-T6 aluminium with the geometry shown in Fig. 15.

This component was manufactured to test the previously mentioned hypothesis raised initially in Section 2.2, that FGWs like those of their flat plate counterparts would be generated in a component where the thickness changes abruptly to a consistent value at the topological feature of interest. These experiments also confirmed if the angle-incidence technique was a viable transduction method in creating Lamb-like FGWs, as theorised in Section 2.3. To prove these two points, the material used was not of concern and aluminium was selected due to its low attenuation and scattering properties. The geometry was also further simplified to remove the presence of air gaps in the side plates due to time and economic constraints. Therefore, it was expected that only Lamb-like wave modes would be created in the centre 5 mm thick pseudo weld region.

A Perspex wedge with a 30-degree angle was machined and is shown

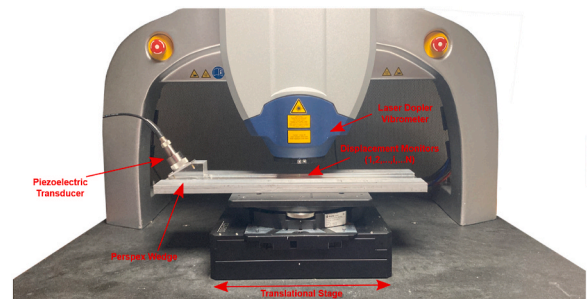


Fig. 16. Pseudo weld experimental set up.

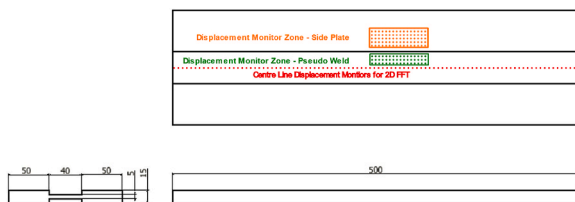


Fig. 15. Pseudo weld 3rd angle projection schematic in mm.

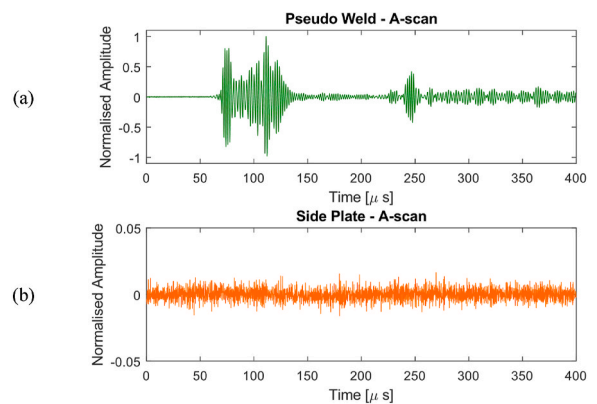


Fig. 17. A-Scans from pseudo weld and side sheets (a) A-scan on 5 mm thick pseudo weld (b) A-scan on 15 mm thick side sheet.

along with the experimental set-up in Fig. 16. As this experiment was intended to show that Lamb waves are only generated in the pseudo weld, the angle of the wedge was not optimised. A commercially available Olympus, 1-inch diameter, piezoelectric transducer (Part No: A301S-SU, Item Number U8421001) was pulsed with a 5-cycle Hann-windowed wave at 500 kHz using the Wavemaker Duet pulser from Macro Design Ltd. Gel couplant [40] was applied between the transducer and wedge as well as between the wedge and sample. Two displacement monitoring zones were set up: one on the pseudo weld and the other on the thicker side plates. The displacement in both zones was monitored using a Polytec MSA-100-3D laser Doppler vibrometer, animated and is available via the supplemental data provided. It can clearly be seen that there is a strong wavefront generated only within the pseudo weld region. Only noise is present in the thicker side sheets. Fig. 17 shows A-scans from the pseudo weld and thicker side sheets normalised to the maximum value observed across both signals. Again, it can be seen that a strong wavefront is generated in the welded region with only noise present in the thicker side sheets. This result gives a strong indication that a flexible FGW had been successfully generated.

To further confirm and expand our findings, the same piezoelectric transducer was pulsed with a 5-cycle Hann-windowed wave packet from 200 kHz to 900 kHz in steps of 100 kHz. For each frequency, the Polytec MSA-100-3D laser Doppler vibrometer monitored the centre line displacements along the weld from 200 to 300 mm in front of the

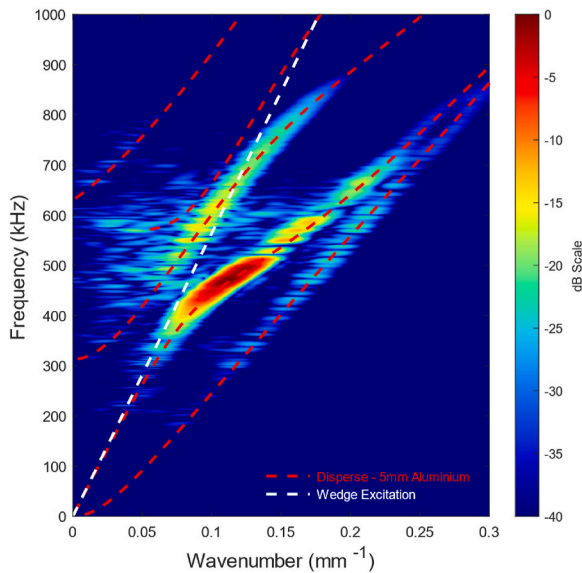


Fig. 18. Wavenumber-frequency spectra for superimposed data on the pseudo weld.

transducer location in steps of 0.3 mm. Each signal was normalised and superimposed at each location, creating one array of displacements for all frequencies. The resulting array was analysed using the aforementioned 2D-FFT method and compared to the Lamb wave analytical solutions for a 5 mm thick aluminium free plate generated by the computational solver, Disperse [41], in Fig. 18.

Fig. 18 shows strong alignment between the experimental data and analytical solutions. It is noted that due to the frequency-thickness product at 500 kHz with the unoptimised wedge angle, multiple Lamb wave modes are excited. Furthermore, the amplitude observed in the spectra increases as the dispersion curves approach the wedge's excitation curve and the transducer's centre frequency. This result confirms that the angle-incidence method is a suitable transduction technique to excite flexural Lamb-like FGWs.

These observations also have broader implications that could be exploited. For example, other similar structures that contain flat plate-like features could use the dispersion relationships from analytical solvers (i.e. Disperse [41], GUIGUW [42]), avoiding the need to run a complex SAFE model to predict, excite and launch FGWs of their own. Hence, this approach could be applicable to I-beam structures and other similar metallic extrusions.

3.2. Resistance seam weld

3.2.1. PTFE wedges

With confidence in the transduction technique, further vibrometry and pulse-echo experiments on flat and curved canister-like RSW samples were conducted. A pulse-echo experimental set-up was chosen to be integrated as it is believed to best mimic a real-world inspection scenario where access to complex equipment, like a laser Doppler vibrometer, is cost-prohibitive. To facilitate these experiments, two wedges were manufactured with and without a curved bottom surface from PTFE with a 30-degree angle to conform to the angle-incidence transduction formula. The wedges are shown in Fig. 19.

PTFE was chosen due to its low longitudinal wave speed of $\sim 1,400$ m/s and the low F_0 phase velocity of 2524 m/s at 1 MHz, making any resulting wedge easily manufacturable. The angle-incidence method is described mathematically in Eq. (5), where v_l is the longitudinal speed of sound of the wedge and v_{ph} is the phase velocity of the guided wave being excited.

$$\theta = \sin^{-1} \left(\frac{v_l}{v_{ph}} \right) \quad \text{Eq. 5}$$

Both wedges feature a polyurethane-based AptFlex F48A absorber (see Fig. 22) from Precision Acoustics [43] to limit any amount of reflected sound within the wedge interfering with the signal from the sample itself.

To confirm the performance of the wedge and absorber, a simple A-

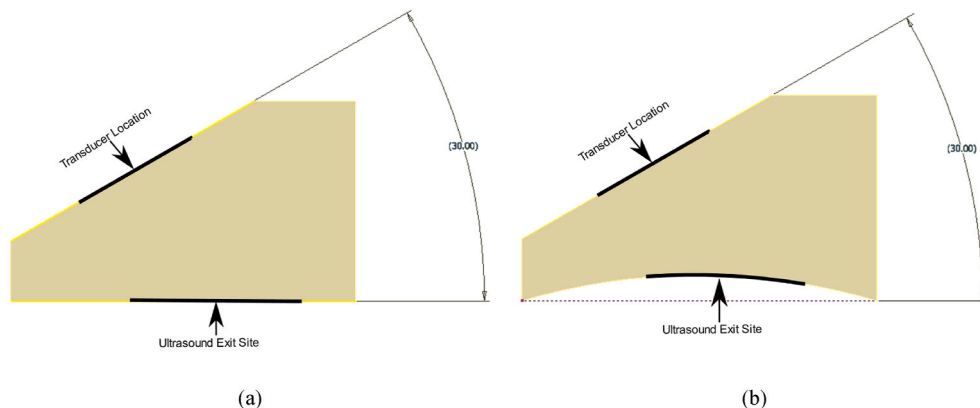


Fig. 19. Schematic of PTFE wedge (a) PTFE wedge for flat RSW samples, (b) PTFE wedge for curved canister-like RSW samples.

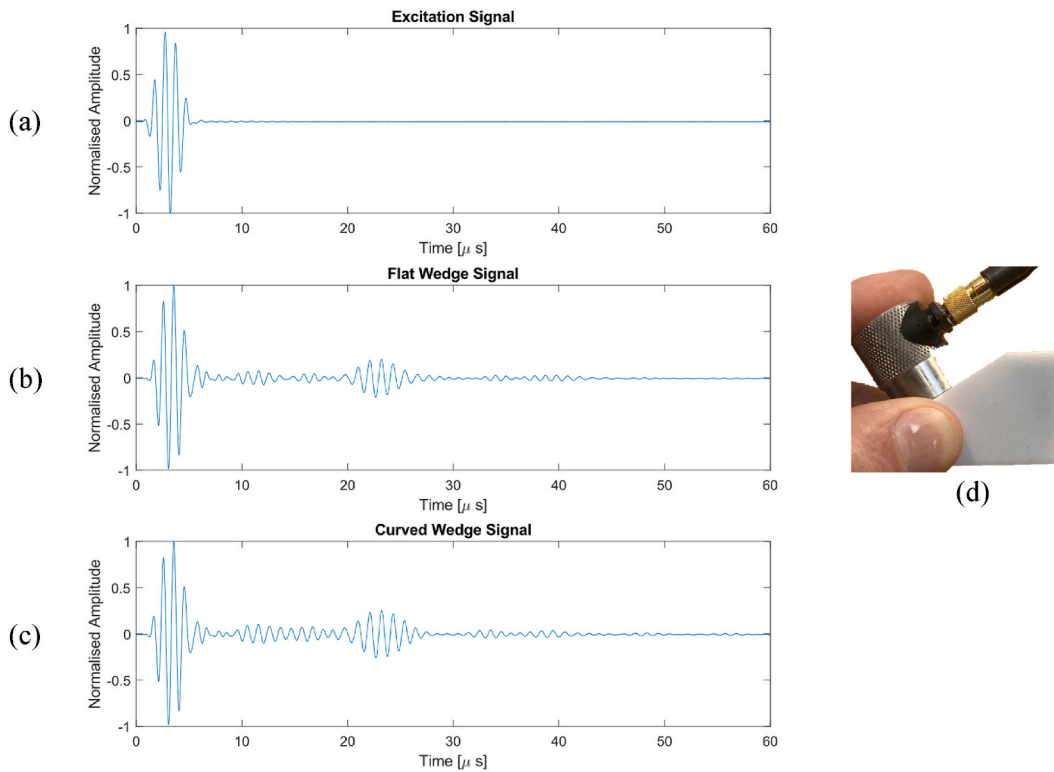


Fig. 20. Illustration of simple wedge A-scan experiment, (a) Normalised 1 MHz 5-cycle Hann windowed excitation signal, (b) Normalised A-scan from flat bottomed wedge held in air, (c) Normalised A-scan from curved bottom wedge held in air, (d) Photo of simple experimental set-up.

scan into air was performed. A commercially available Olympus, 0.5-inch diameter, dual-element piezoelectric transducer (Part No: DHC703-RM, Item Number: U8452055) was excited with a 1 MHz 5-cycle Hann-windowed wave packet in a pulse-echo configuration. This dual-element transducer was selected due to its lower ring down in a pitch-catch configuration when compared to an equivalent single-element transducer in a pulse-echo configuration. In addition, the effects of any electromagnetic interference present in the pulser's

electronic systems are also significantly reduced with the transmit and receive channels separated. The receiver had 40 dB amplification, and A-scans with 64 averages at a sampling rate of 100 MHz were acquired via a standard oscilloscope (Tektronix DPO 4054B). Gel couplant [40] was applied between the transducer and wedge as well as between the wedge and sample.

Fig. 20 shows A-scans of the excitation signal, the received A-scan from the flat wedge, and the received signal from the curved wedge, along with a snapshot of the experimental set up. Reverberations are denoted for the first 60 μ s. As a result, multiple peaks are expected to be observed from any interaction with defects, back wall reflections, and full circumferential transits. These reverberations are not expected to be an issue to effectively screen RSW joints and highlight areas for further in-depth inspection via other NDT modalities, as it is envisaged that there will always be sufficient spatial resolution from the transducer to the defect location. This is also shown to be the case with other similar studies in literature [19]. The reverberations observed may be further suppressed, if necessary, via more advanced transducer and wedge design and are the subject of future work.

3.2.2. Flat plate Resistance seam welds

To confirm the dispersive relationship of the RSW joint, a further vibrometry experiment was undertaken on flat RSW samples. The RSW samples comprised of two 0.9 mm thick long 316 stainless steel sheets fused together to a standard used in fabricating canisters. Due to size and economic constraints, the sample used in this experiment was only 200 mm in length. A series of displacement arrays were gathered from 200 kHz to 900 kHz in steps of 100 kHz from 50 mm to 150 mm in front of the transducer in steps of 0.3 mm. As before, each signal was normalised, superimposed, and analysed via the 2D-FFT technique. Fig. 21 shows the resulting frequency wavenumber spectra normalised against the maximum amplitude in a dB scale.

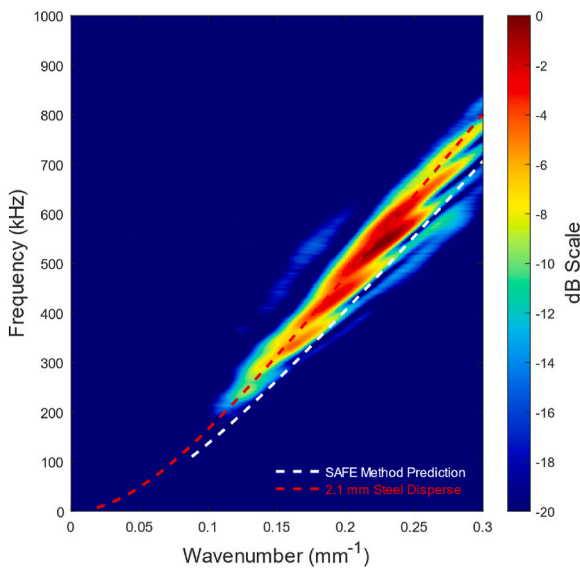


Fig. 21. Wavenumber-frequency spectra for superimposed data on a flat RSW sample.

It can be seen in Fig. 21 that the predicted SAFE results are offset from the experimental data, and the experimental data more closely aligns with the analytical solution for a 2.1 mm steel free plate. The thickness of the analytical solutions was iteratively changed while keeping the material properties constant until good agreement was observed between experimental and analytical datasets. This shift is thought to be due to the undulating nature of the RSW (see Fig. 2(b)), which could not be modelled by the SAFE method. However, even with this slight shift, it can be seen that one flexural mode is excited in the RSW.

With the real-world dispersion relationship better understood, experiments were conducted on flat 0.9-m long RSWs with and without defects. For the defective samples, the defects were represented by a 6.5 mm wide (x_1 direction) by 0.5 mm tall (x_3 direction) through-thickness and 1 mm deep (x_2 direction) transverse EDM notches at an axial position of 500 mm. The receiver had 40 dB amplification, and A-scans with 64 averages were acquired at a sampling frequency of 100 MHz for both defective and defect free flat RSW samples. Gel couplant [40] was applied between the transducer and wedge as well as between the wedge and sample.

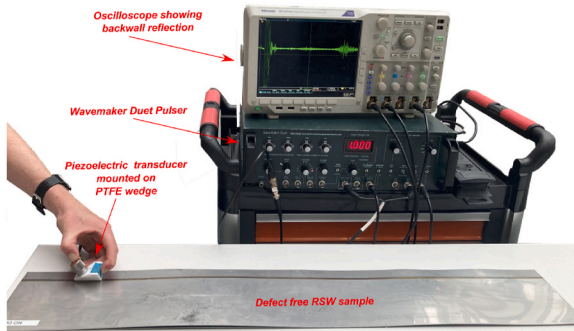


Fig. 22. Experimental set up on a defect-free flat RSW sample.

Fig. 23 shows the resulting A-scans, with strong reflections observed in both the through wall and 1.0 mm defective time series at $\sim 375 \mu s$ along with a significantly dampened back wall reflection. It is also noted that the back wall is observed in the defect free time trace to occur at $\sim 700 \mu s$, giving a velocity of $\sim 2,500$ m/s in agreement with the predicted velocities stated in Section 2.2. All signals were normalised to the maximum amplitude observed after the first 60 μs reverberation zone detailed in Section 3.2.1.

The signal to noise ratios (SNRs) for both defective time series was calculated by computing the ratio of the summed squared magnitude of the signal to that of the noise. First, an envelope was calculated over the entire signal using local maxima separated by 900 samples. The signal was taken to be the signal amplitude between where the envelope value drops to 25% on either side of the maximum envelope value reported at $\sim 375 \mu s$. While the noise was taken to be an equal number of samples as the signal beginning 150 μs . SNRs of 16.33 dB and 8.21 dB were reported for the through wall and 1.0 mm deep defects, respectively. Measurements were also attempted against 0.5 mm and 0.25 mm deep defects, but the reflection was not readily distinguishable from the noise floor. This serves to indicate a practical limit of the technique that may be addressed in future work. Furthermore, with reference to Table 1 this result also indicates that the “half depth” defects modelled are close to the practical limit of the hardware used in this experiment. However, defects of ≥ 1 mm can be clearly seen in the defective time series, demonstrating the efficacy of using this flexural FGW mode to screen for defects on flat RSW plates.

3.2.3. Cylindrical resistance seam weld

Expanding upon the flat plate experiments, cylindrical RSWs were experimented on with and without a defect. Like with the flat RSW samples, a 6.5 mm wide by 0.5 mm tall by 1.0 mm deep transverse EDM notch was created to represent a crack in one location of the cylindrical samples, as it was shown to be the smallest detectable defect. Care was taken in the position of the transducer relative to the EDM notch to avoid mistaking a full circumferential transit as a defect located diametrically opposite the transducer location. As a result, the transducer was

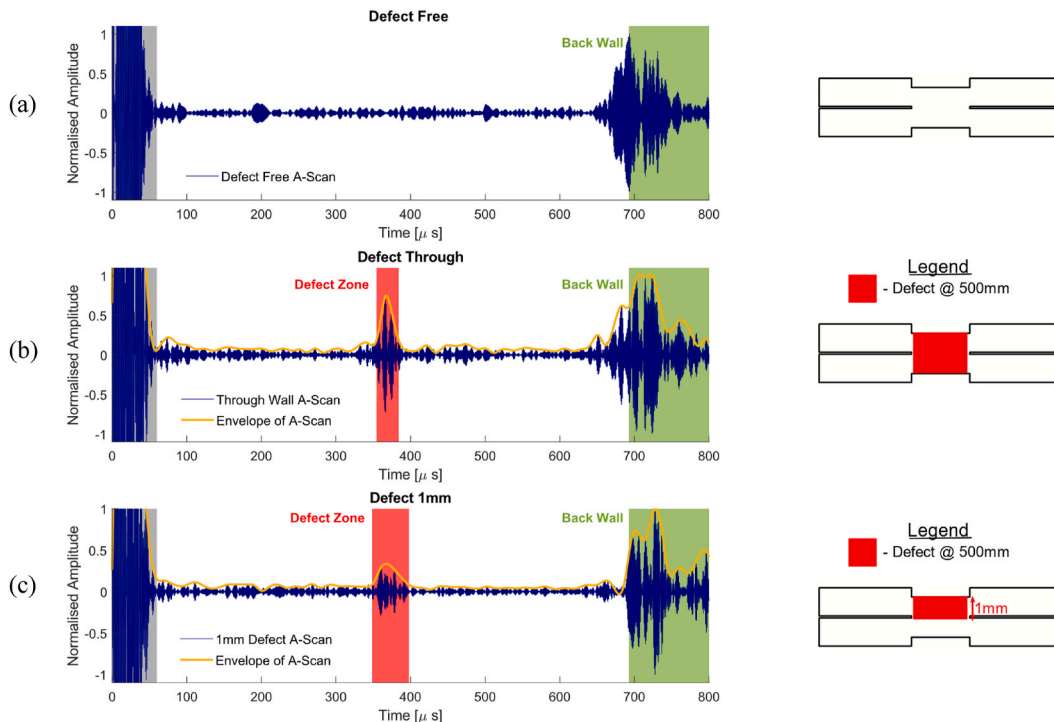


Fig. 23. Normalised A-Scans on defect-free and defective flat plate RSW samples (a) Normalised A-scan for a defect-free flat RSW sample, (b) Normalised A-scan for a through wall defective flat RSW sample, (c) Normalised A-scan for a 1 mm deep defective flat RSW sample.

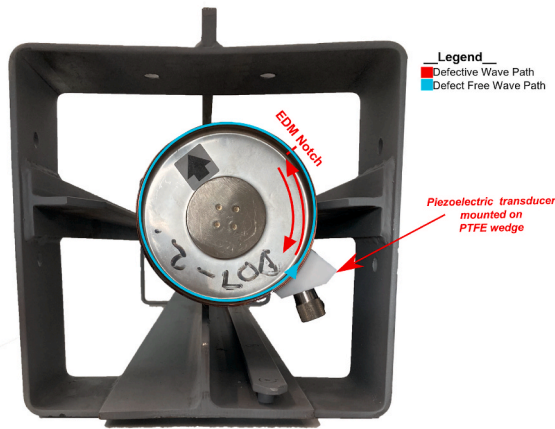


Fig. 24. Experimental set up on cylindrical RSW.

positioned at approximately a quarter of the circumference from the EDM notch. The same 1 MHz Olympus transducer (Part No: DHC703-RM, Item Number: U8452055) was pulsed with a 5-cycle 1 MHz Hann-windowed wave packet, and A-scans were collected with 64 averages at a sampling frequency of 100 MHz and 40 dB of amplification. Gel couplant [40] was applied between the transducer and wedge as well as between the wedge and sample. The experimental set up is shown in Fig. 24.

Fig. 25 shows the acquired A-scans for defect-free and defective cylindrical RSWs. In the defect-free time series, a full circumferential transit is observed at $\sim 180 \mu s$. In the defective time series at $\sim 115 \mu s$, a strong reflection is observed from the EDM notch and is accompanied by a large reduction in the full circumferential transit. Like in Section 3.2.2, the SNR of the defective time series was calculated. An envelope was

calculated over the full signal using local maxima separated by 450 samples. The signal was taken to be the signal amplitude between where the envelope value drops to 25% on either side of the maximum envelope value reported at $\sim 115 \mu s$. While the noise was taken to be an equal number of samples as the signal beginning at $180 \mu s$. A SNR of 11.85 dB was reported and is in good agreement with the SNR reported to the same 1.0 mm deep defect in Section 3.2.2. Additional samples with defects at different positions were not possible due to sample availability but will be considered as part of future work.

It is also noted that to provide full circumferential coverage, two inspection locations are required. If only one inspection location is utilised, 'blind spots' are created by the transducer ring-down time from the wedge into the sample and from a defect diametrically opposite from the transducer location, which could appear as a full circumferential transit.

Regardless of these two limitations, it is clear from the acquired data that this technique could be used to screen the quality of RSWs whilst in storage and facilitate further detailed inspection of any defective welds identified.

4. Concluding remarks

It has been shown in other publications that FGWs have been effectively used to screen fusion welds, seal fins, rolled plate, and adhesive joints. This paper presents for the first time the use of anti-symmetric FGWs to effectively screen RSWs that are used within the nuclear industry.

FGWs have been investigated for the targeted screening of nuclear grade RSW joints through the SAFE method. Four weld-guided wave modes were identified. Through down selection, the fundamental flexural (F0) weld guided mode, with the average power flow ratio on average 5.25 times higher than the next highest wave mode, was selected for further study. Several FE models were developed and confirmed the prediction from the SAFE model that a flexural FGW

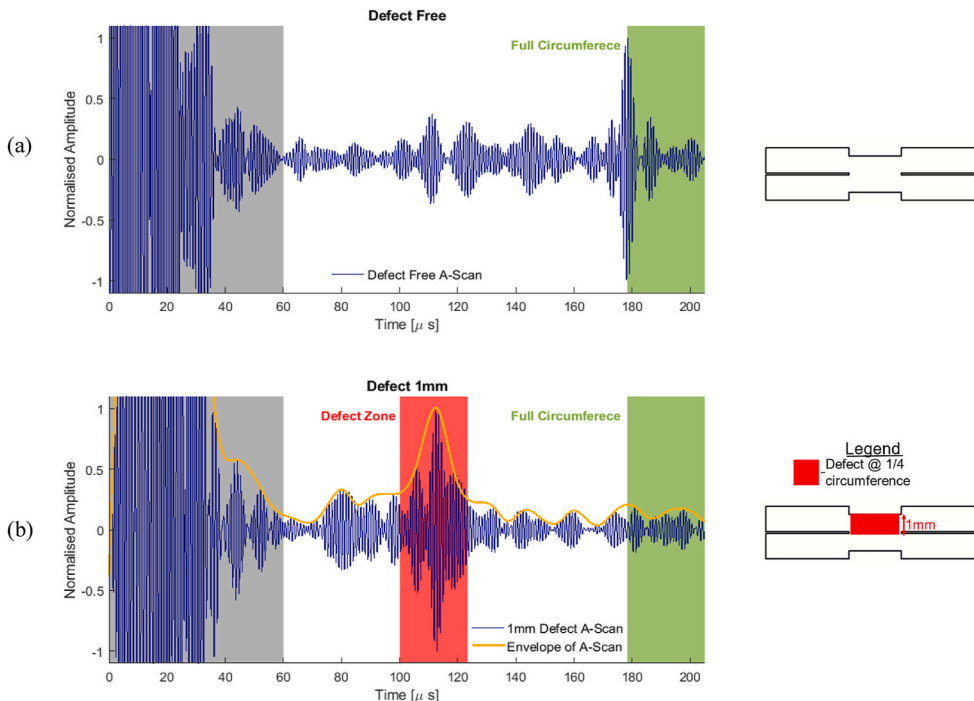


Fig. 25. A-Scans on defect-free and defective cylindrical RSWs.

would exist within the RSW. Furthermore, the FE models also investigated the defect sensitivity of the F0 mode to transverse cracks concluding that the defect depth was the primary driver behind strong reflections. Several experiments were conducted on defective and defect-free pseudo RSW structures, flat plate and cylindrical RSWs. For the pseudo weld experiments, it was shown that FGWs, like that of the analytical free plate counterparts, could easily be excited in flat plate-like features with traditional transduction techniques. For the flat plate RSW experiments, it was shown that reflections from through wall and 1.0 mm deep defects could be observed with SNRs of 16.33 dB and 8.21 dB being respectively reported. Lastly, it was shown that for cylindrical canister like RSWs, reflections could also be observed from 1.0 mm deep defects with a SNR of 11.85 dB being reported. These results show the potential of using flexural FGWs to screen RSW joints.

In future work, the authors plan to improve and progress this study: by: 1) performing a parametric analysis on the RSW geometry and study how changes in geometry affect the wave propagation; 2) increasing the accuracy of simulated efforts to better match real-world observations and; 3) improving the wedge and transducer design to lower reverberations in order to decrease the size of the minimal detectable defect size. The authors also plan to explore the use of FGWs to rapidly screen RSWs, locate defects, and automatically raster scan any areas identified from the screening technique with a more in-depth local NDT modality.

Author statement

Euan Foster: Conceptualization, methodology, data curation, writing, original draft preparation, reviewing and editing.

Charles MacLeod: Supervision, reviewing and editing, methodology.

Ehsan Mohseni: Supervision, reviewing.

Anthony Gachagan: Supervision, reviewing.

Robert Bernard: Supervision, reviewing.

Gary Bolton Bernard: Supervision, reviewing.

Declaration of competing interests

The authors declare that they have no known competing financial interests or personal relationships that could have appeared to influence the work reported in this paper.

Acknowledgements

This work is supported by the Research Centre for Non-Destructive Evaluation (RCNDE) on behalf of Sellafeld Ltd and NNL Ltd in the UK under EPSRC Grant No: EP/L015587/1.

We would like to thank Dr. Xudong Yu of Beihang University, Dr. Zheng Fan of Nanyang Technological University, Dr. Peter Huthwaite & Professor Michael Lowe of Imperial College London, and Michel Castaings of Institut Polytechnique de Bordeaux for their help and useful discussions.

The data, key files, and illustrations that support the findings of this study can be found at the University of Strathclyde KnowledgeBase repository - DOI <https://doi.org/10.15129/9d70d515-b93e-4246-8feb-a4877b286b6d>.

Appendix A. Supplementary data

Supplementary data to this article can be found online at <https://doi.org/10.1016/j.ndteint.2022.102695>.

References

- [1] Jenney CL, O'Brien A. *Welding Society American. Welding handbook committee. Welding handbook*. Miami, FL: American Welding Society; 2001.
- [2] Ouissse M, Cogan S. Robust design of spot welds in automotive structures A decision-making methodology. *Mech Syst Signal Process* 2010;19. <https://doi.org/10.1016/j.ymssp.2009.09.012>.
- [3] Fakh MA. Detection and assessment of flaws in friction stir welded joints using ultrasonic guided waves: experimental and finite element analysis. *Mech Syst Signal Process* 2018;19. <https://doi.org/10.1016/j.ymssp.2017.09.003>.
- [4] Eisazadeh H, Hamed M, Halvae A. New parametric study of nugget size in resistance spot welding process using finite element method. *Mater Des* 2010;31: 149–57. <https://doi.org/10.1016/j.matdes.2009.06.042>.
- [5] Qiuyue F, Guocheng X, Xiaopeng G. Ultrasonic nondestructive evaluation of porosity size and location of spot welding based on wavelet packet analysis. *J Nondestr Eval* 2020;39:7. <https://doi.org/10.1007/s10921-019-0650-1>.
- [6] Kong J-P, Kang C-Y. Effect of alloying elements on expulsion in electric resistance spot welding of advanced high strength steels. *Sci Technol Weld Join* 2016;21: 32–42. <https://doi.org/10.1179/1362171815Y.0000000057>.
- [7] Mira-Aguar T, Galvão I, Leitão C, Rodrigues DM. Analysis of weld defects in similar and dissimilar resistance seam welding of aluminium, zinc and galvanised steel. *Sci Technol Weld Join* 2015;20:409–17. <https://doi.org/10.1179/1362171815Y.0000000031>.
- [8] Kroening M, Sednev D, Chumak D. *Nondestructive testing at nuclear facilities as basis for the 3S synergy implementation*. IEEE; 2012. p. 1–4.
- [9] Hyatt NC. Plutonium management policy in the United Kingdom: the need for a dual track strategy. *Energy Pol* 2017;101:303–9. <https://doi.org/10.1016/j.enpol.2016.08.033>.
- [10] Lowe M, Cawley P. Long range guided wave inspection usage – current commercial capabilities and Research directions. 2007. <http://www3.imperial.ac.uk/pls/porta/llive/docs/1/55745699.PDF>. [Accessed 3 November 2019].
- [11] Sargent JP. Corrosion detection in welds and heat-affected zones using ultrasonic Lamb waves. *Insight - Non-Destr Test Cond Monit* 2006;48:160–7. <https://doi.org/10.1784/insi.2006.48.3.160>.
- [12] Fan Z, Lowe MJS. Elastic waves guided by a welded joint in a plate. *Proc R Soc Math Phys Eng Sci* 2009;465:2053–68. <https://doi.org/10.1098/rspa.2009.0010>.
- [13] Fan Z. *Applications of guided wave propagation on waveguides with irregular cross-section*. PhD Thesis. Imperial College London; 2010.
- [14] Fan Z, Lowe MJS. Interaction of weld-guided waves with defects. *NDT E Int* 2012; 47:124–33. <https://doi.org/10.1016/j.ndteint.2012.01.001>.
- [15] Yu X, Zuo P, Xiao J, Fan Z. Detection of damage in welded joints using high order feature guided ultrasonic waves. *Mech Syst Signal Process* 2019;126:176–92. <https://doi.org/10.1016/j.ymssp.2019.02.026>.
- [16] Ramdhas A, Pattanayak RK, Balasubramaniam K, Rajagopal P. Antisymmetric feature-guided ultrasonic waves in thin plates with small radius transverse bends from low-frequency symmetric axial excitation. *J Acoust Soc Am* 2013;134: 1886–98. <https://doi.org/10.1121/1.4817878>.
- [17] Manogharan P, Yu X, Fan Z, Rajagopal P. Interaction of shear horizontal bend (SHB) guided mode with defects. *NDT E Int* 2015;75:39–47. <https://doi.org/10.1016/j.ndteint.2015.06.004>.
- [18] Manogharan P, Rajagopal P, Balasubramaniam K. Longitudinal guided waves confined in radius filler regions of composite joints. *J Acoust Soc Am* 2016;140: 334–43. <https://doi.org/10.1121/1.4955288>.
- [19] Corcoran J, Leinov E, Jeketo A, Lowe MJS. A guided wave inspection technique for wedge features. *IEEE Trans Ultrason Ferroelectrics Freq Control* 2020;67: 997–1008. <https://doi.org/10.1109/TUFFC.2019.2960108>.
- [20] Yu X, Fan Z, Castaings M, Biateau C. Feature guided wave inspection of bond line defects between a stiffener and a composite plate. *NDT E Int* 2017;89:44–55. <https://doi.org/10.1016/j.ndteint.2017.03.008>.
- [21] Auld BA. *In: Acoustic fields and waves in solids*. second ed., vol. 1. Malabar, Florida: Krieger Publishing Company; 1973.
- [22] Zuo P, Fan Z. SAFE-PML approach for modal study of waveguides with arbitrary cross sections immersed in inviscid fluid. *J Sound Vib* 2017;406:181–96. <https://doi.org/10.1016/j.jsv.2017.06.001>.
- [23] Castaings M, Lowe M. Finite element model for waves guided along solid systems of arbitrary section coupled to infinite solid media. *J Acoust Soc Am* 2008;123: 696–708. <https://doi.org/10.1121/1.2821973>.
- [24] COMSOL 5.6 multiphysics reference manual n.d. <https://doc.comsol.com/> (accessed November 3, 2021).
- [25] Rose JL. *Ultrasonic guided waves in solid media*. New York: Cambridge University Press; 2014. <https://doi.org/10.1017/CBO9781107273610>.
- [26] Choi S, Cho H, Lissenden CJ. Nondestructive inspection of spent nuclear fuel storage canisters using shear horizontal guided waves. *Nucl Eng Technol* 2018;50: 890–8. <https://doi.org/10.1016/j.net.2018.04.011>.
- [27] Luo W, Zhao X, Rose JL. A guided wave plate experiment for a pipe. *J Pressure Vessel Technol* 2005;127:345. <https://doi.org/10.1115/1.1989351>.
- [28] Zuo P, Yu X, Fan Z. Numerical modeling of embedded solid waveguides using SAFE-PML approach using a commercially available finite element package. *NDT E Int* 2017;90:11–23. <https://doi.org/10.1016/j.ndteint.2017.04.003>.
- [29] Nguyen KL, Treysède F, Hazard C. Numerical modeling of three-dimensional open elastic waveguides combining semi-analytical finite element and perfectly matched

- layer methods. *J Sound Vib* 2015;344:158–78. <https://doi.org/10.1016/j.jsv.2014.12.032>.
- [30] Ledbetter HM. Monocrystal elastic constants in the ultrasonic study of welds. *Ultrasonics* 1985;23:9–13. [https://doi.org/10.1016/0041-624X\(85\)90005-8](https://doi.org/10.1016/0041-624X(85)90005-8).
- [31] Huthwaite P. Accelerated finite element elastodynamic simulations using the GPU. *J Comput Phys* 2014;257:687–707. <https://doi.org/10.1016/j.jcp.2013.10.017>.
- [32] Combaniere J, Cawley P, McAughy K, Giese J. Interaction between SH0 guided waves and tilted surface-breaking cracks in plates. *IEEE Trans Ultrason Ferroelectrics Freq Control* 2019;66:119–28. <https://doi.org/10.1109/TUFFC.2018.2876723>.
- [33] De Luca A, Perfetto D, De Fenza A, Petrone G, Caputo F. Guided waves in a composite winglet structure: numerical and experimental investigations. *Compos Struct* 2019;210:96–108. <https://doi.org/10.1016/j.compstruct.2018.11.048>.
- [34] Ma Y, Yang Z, Zhang J, Liu K, Wu Z, Ma S. Axial stress monitoring strategy in arbitrary cross-section based on acoustoelastic guided waves using PZT sensors. *AIP Adv* 2019;9:125304. <https://doi.org/10.1063/1.5130723>.
- [35] Drozd MB. Efficient finite element modelling of ultrasound waves in elastic media. *PhD Thesis. Imperial College London (University of London); 2008*.
- [36] Alleyne D, Cawley P. A two-dimensional Fourier transform method for the measurement of propagating multimode signals. *J Acoust Soc Am* 1991;89:1159–68. <https://doi.org/10.1121/1.400530>.
- [37] Wilcox PD, Lowe MJS, Cawley P. Mode and transducer selection for long range Lamb wave inspection. *J Intell Mater Syst Struct* 2001;12:553–65. <https://doi.org/10.1177/10453890122145348>.
- [38] Dobie G, Hayward G, Pierce G. Ultrasonic sensor platforms for non-destructive evaluation. *PhD Thesis. University of Strathclyde; 2010*.
- [39] Van Pamel A. Ultrasonic inspection of highly scattering materials. *PhD Thesis. Imperial College London; 2015*.
- [40] SuperSoniX™ - highest performance ultrasonic couplant - Echo Ultrasonics. <https://www.echoultrasonics.com/product/supersonix-ultrasonic-couplant/> (accessed June 2, 2022).
- [41] Pavlakovic B, Lowe M, Alleyne D, Cawley P. Disperse: a general purpose program for creating dispersion curves. In: Thompson DO, Chimenti DE, editors. *Rev. Prog. Quant. Nondestruct. Eval.* Boston, MA: Springer US; 1997. p. 185–92. https://doi.org/10.1007/978-1-4615-5947-4_24.
- [42] Bocchini P, Marzani A, Viola E. Graphical user interface for guided acoustic waves. *J Comput Civ Eng* 2011;25:202–10. [https://doi.org/10.1061/\(ASCE\)CP.1943-5487.0000081](https://doi.org/10.1061/(ASCE)CP.1943-5487.0000081).
- [43] Aptflex F48. Precision Acoustics n.d. <https://www.acoustics.co.uk/product/aptflex-f48/> (accessed April 21, 2022).